



This is a repository copy of *Variation of texture anisotropy and hardness with build parameters and wall height in directed-energy-deposited 316L steel.*

White Rose Research Online URL for this paper:
<http://eprints.whiterose.ac.uk/169707/>

Version: Published Version

Article:

Chechik, L., Boone, N.A. orcid.org/0000-0002-5251-0104, Stanger, L.R. orcid.org/0000-0003-4853-1399 et al. (5 more authors) (2021) Variation of texture anisotropy and hardness with build parameters and wall height in directed-energy-deposited 316L steel. *Additive Manufacturing*, 38. 101806. ISSN 2214-8604

<https://doi.org/10.1016/j.addma.2020.101806>

Reuse

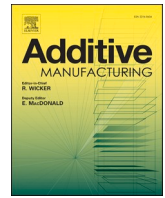
This article is distributed under the terms of the Creative Commons Attribution (CC BY) licence. This licence allows you to distribute, remix, tweak, and build upon the work, even commercially, as long as you credit the authors for the original work. More information and the full terms of the licence here:
<https://creativecommons.org/licenses/>

Takedown

If you consider content in White Rose Research Online to be in breach of UK law, please notify us by emailing eprints@whiterose.ac.uk including the URL of the record and the reason for the withdrawal request.



eprints@whiterose.ac.uk
<https://eprints.whiterose.ac.uk/>



Variation of texture anisotropy and hardness with build parameters and wall height in directed-energy-deposited 316L steel

Lova Chechik^{a,*}, Nicholas Andrew Boone^b, Leigh Russell Stanger^b, Peter Honniball^c, Felicity Freeman^a, Gavin Baxter^d, Jon Raffae Willmott^b, Iain Todd^a

^a Department of Materials Science and Engineering, The University of Sheffield, Mappin Street, S1 3JD, UK

^b Department of Electronic and Electrical Engineering, The University of Sheffield, Mappin Street, S1 3JD, UK

^c Rolls-Royce plc, PO Box 2000, Derby DE24 7XX, UK

^d Rolls-Royce plc, PO Box 31, Derby DE24 8BJ, UK

ARTICLE INFO

Keywords:

Directed Energy Deposition
Thermal imaging
Grain structure
Texture

ABSTRACT

Directed energy deposition (DED) is an emerging technology with repair applications in critical aerospace components. Mechanical properties of DED components have been shown to vary significantly through a part, making it difficult to achieve the level of process control required for these applications. Using thermal data captured in-situ, cooling rates and melt pool dimensions were calculated and related to the final grain structure, captured by EBSD. The changes in cooling rate explain the microstructural variation between different processing parameters and through the build height. A new approach, using a cumulative anisotropy factor was implemented and correlates the variation in hardness with grain structure. Two regimes were found depending on the linear heat input in 316L, with high linear heat input resulting in great amounts of mechanical anisotropy on the component level. The relationships between thermal signature and mechanical properties suggest close control of anisotropy could be achieved by monitoring and controlling the melt pool size using a coaxial camera.

1. Introduction

Laser Directed Energy Deposition (DED), is a branch of metal additive manufacturing (AM) where components are created layer-by-layer. The focus of this paper will be on blown powder laser DED in which a powder feedstock is deposited into a molten pool created by a laser. This process experiences rapid cooling, with cooling rates estimated on the order of 10^3 – 10^4 K/s, significantly quicker than traditional manufacturing processes [1]. DED has been implemented with a range of alloys, including Inconel 718 [2], Al 4047 [3] and 316L stainless steel [4,5], the latter being the focus of this paper.

A key advantage of DED is the capability to repair a pre-existing component, e.g. gas turbines and to build complex freeform components [6–8]. The microstructure depends on the cooling rate and the thermal gradient; slight variations in the process or part geometry make it difficult to achieve the high level of microstructural control required [9].

To reduce both time and materials waste when optimising a process, significant effort has been invested in thermal modelling of various laser

processes, including laser welding and DED [10,11]. The melt pool width in DED is typically 1 mm, much larger than that in other laser AM processes e.g. 0.1 mm in powder bed fusion [4,12]. Due to the large melt pool size, the maximum heat flow and so the solidification direction lies in the plane tilted between the build direction and the laser movement direction [13,14]. Depending on the laser raster pattern and the processing parameters, this angle is 45–60° above the horizontal [2,13]. Welding solidification models predict grains to sweep radially from the melt pool edges. With higher input power, these grains get swept along the laser movement direction. Where these sweeping grains from the edges meet, a centreline can be formed [10,15].

In DED, this centreline is predicted to contain many small grains, with long grains spanning between adjacent laser centre locations. As velocity is increased, the centreline region widens, changing the texture [11]. A strong texture is found in the build plane perpendicular to the laser movement, as explained by elongated grains growing between laser centre lines. Secondary texture is found between the laser movement direction and the build direction, corresponding to the maximum thermal gradients. In a bidirectional raster system, this will lead to a less

* Corresponding author.

E-mail address: lchechik1@sheffield.ac.uk (L. Chechik).

<https://doi.org/10.1016/j.addma.2020.101806>

Received 12 August 2020; Received in revised form 14 December 2020; Accepted 19 December 2020

Available online 29 December 2020

2214-8604/© 2021 The Authors. Published by Elsevier B.V. This is an open access article under the CC BY license (<http://creativecommons.org/licenses/by/4.0/>).

intense texture, as there are two equally significant crystal directions [2, 15]. This phenomenon is commonly referred to as a solidification fibre texture [2,3,14].

Due to the change in heat flow conditions with build height, the cooling rates change and a different microstructure is achieved [16,17]. This variation of mechanical properties with height has been reported through mechanical testing including hardness [18]. Additionally, when subsequent layers are printed, the deposited material is reheated multiple times. This leads to the bulk experiencing similar conditions, but a different microstructure in the final 1–2 mm of the build due to lack of reheating [19].

Mechanical properties of a part are controlled by the grain structure. Both hardness and elastic modulus vary by 20% depending on the crystal orientation [20]. An anisotropy value has been defined, which varies between 0 for <100> directions to 1/3 for <111> directions [21]:

$$A_{hkl} = \frac{h^2k^2 + k^2l^2 + l^2h^2}{(h^2 + k^2 + l^2)^2} \quad (1)$$

Stinville et al. reported hardness to increase linearly with the anisotropy value in polycrystalline 316L [20]. Similar findings have been found in another austenitic stainless steel (301LN), with a higher variance [22].

In literature, Schmid factors have been used to correlate hardness to microstructure for a Berkovich indenter. Specific slip plane observations were required, limiting the transferability of this technique, but by combining 6 Schmid factors, a good correlation was achieved [23]. The Taylor factor has also been reported to describe the orientation dependence of nanoindenter hardness [24]. These studies used nanoindentation of individual grains. Care must be taken when comparing absolute hardness values due to the indentation size effect, which causes measured hardness to decrease as indenter load increases [25]. When macroscopic properties are of interest, larger indents are more representative due to the averaging of multiple grains, although this likely reduces the hardness difference between measurements. To the authors' knowledge, the dependence of hardness on grain orientation has not been extended to areas covering multiple grains by creating cumulative orientation factors.

The final microstructure strongly depends on the thermal conditions experienced during solidification; cooling rate being the key factor [1, 26,27]. Cooling rate is difficult to measure in-situ, so work has been published relating cooling rate to melt pool dimensions. A linear log-log relationship has been shown between cooling rate and melt pool length [4]. Hence research has focused on measuring melt pool dimensions [5, 28] and relating the dimensions to the microstructure [18].

The melt pool size and dilution are sensitive to the processing parameters such as power, velocity, mass flow [29]. Increasing power or decreasing velocity leading to a larger melt pool [30]. Linear heat input (H) is used as a parameter which encompasses both the laser power and velocity. Linear heat input, $H = P/v$ where P is the laser power (W) and v is the laser velocity (m/s) [1]. Even with a constant H, as the build height increases the heat flow behaviour changes. Conduction to the baseplate is reduced as distance from the baseplate increases, leading to increased melt pool temperature and size through the build [16]. Using coaxial measurement (along the beam direction), the melt pool area has been shown to increase by factors of 1.1–3.0 through a build [5,18,30, 31]. Changes in the melt pool size lead to dimensional variation in the component [5,28].

Previous work has shown there to be differences in thermal signature when varying processing parameters and through the height of a build. The final mechanical properties are affected, but no direct relationship between the microstructure and mechanical properties has been reported for AM. In this study, melt pool size and cooling rate were calculated during manufacture of various walls using DED. Walls were built with linear heat input changing by a factor of 2 to measure the effect of varying processing parameters. The thermal measurements

were related to the microstructure which was characterised through an extension of anisotropy factor which has previously only been used for individual grains. The anisotropy factor was shown to strongly correlate with hardness on a micro-scale. This variation in microstructure was explained in relation to both processing parameters and build height.

2. Materials and methods

2.1. Experimental method

The experimental work was performed on a BeAM Magic 2.0 DED machine. This is fitted with a 2 kW Ytterbium CW laser, beam diameter 0.7 mm. The powder and laser are focused on the substrate, 3.5 mm below the bottom of the nozzle (manufacturer's recommendation). Gas atomised 316L stainless steel powder of size range 45–90 μm (TLS Technik) was used; maintained in the range 7–7.5 g/min. An argon carrier gas provided local shielding at 12 l/min.

Table 1 shows the parameters used to deposit 5 rectangular walls on a 4 mm thick 316L baseplate. Two velocities and two powers were used to provide a factor of 2 range in linear heat input (H); Wall A was duplicated to check repeatability. Fig. 1a shows the geometry of the printed parts; the axes definitions will be used throughout. The walls consisted of 6 bidirectional hatches scanned in the X (laser movement) direction, with 450 μm hatch spacing (in the Y) and 200 μm Z step between layers. 49 layers were printed, with the laser returning to the same start point between layers (3.6 s interlayer time).

YZ wall sections (defined in Fig. 1) were polished before hardness was measured using a Durascan 70 Vickers indenter with a 1 kg load (5 s hold). Between 27 and 30 measurements were taken for each sample, in a $3 \times 9/10$ array (Y and Z respectively). Polished samples were etched with aqua regia before being analysed optically for porosity using ImageJ.

2.2. Electron Backscattered Diffraction (EBSD)

EBSD was performed on polished samples using an FEI Apreo FEG scanning electron microscope. Scans used a 10 μm step size, an accelerating voltage of 20 kV and a probe current of 13 nA. EBSD scans were in the YZ plane. For walls A1, B, C, D (Table 1) scans were taken in the centre (in both Y and Z); Walls A1 and D had further scans taken at the top and bottom (both central in Y).

Analysis was performed using MTEX 5.3.0, an open source MATLAB Toolbox [32]. EBSD scans were cropped to 2 hatches wide (900 μm) and 2 mm tall. Grains were reconstructed with a threshold grain boundary misorientation of 10° , with a minimum of 3 pixels per grain. Grain sizes refer to the equivalent radius calculated from the area of each grain. Schmid factors were calculated in the normal (X) direction as were Taylor factors (compressive strain, 0.1).

2.3. Thermal monitoring

The thermal imaging instrument consisted of a Hamamatsu C12741-03 InGaAs camera [33] and a Thorlabs MVTC23005 telecentric lens. The use of a telecentric lens afforded a thermal image undistorted by perspective, resulting in an isometric projection of the scene. The

Table 1
Processing Parameters.

Sample	Power (W)	Velocity (mm/min)	Hatch spacing (μm)	Z Step (mm)	H (J/mm)
Wall A1	300	2750	450	0.2	6.5
Wall A2	300	2750	450	0.2	6.5
Wall B	300	2250	450	0.2	8.0
Wall C	500	2750	450	0.2	10.9
Wall D	500	2250	450	0.2	13.3

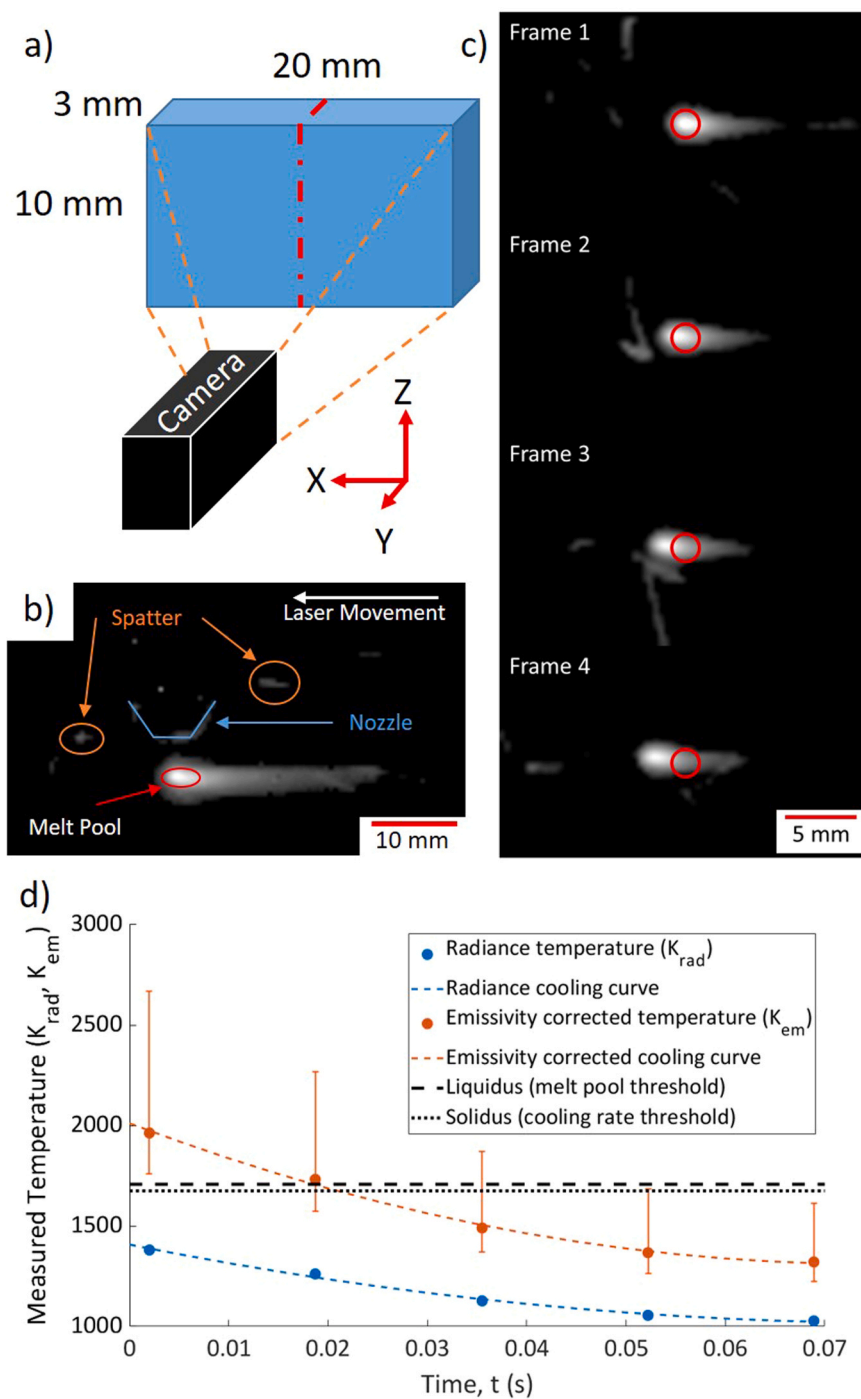


Fig. 1. a) Schematic of deposited walls, showing approximate dimensions and axis definitions. b) Representative thermal image showing key features. c, d show extraction of cooling rate. c) time series of images showing same field of view, temperature taken from centre of red circle. d) Schematic of cooling curves comparing radiance temperature (K_{rad}) with emissivity corrected temperature (K_{em}). Error bars show the uncertainty originating from the emissivity value. Cooling rates calculated at emissivity corrected solidus temperature. (For interpretation of the references to colour in this figure legend, the reader is referred to the web version of this article.)

exposure was set to 16.7 ms, the frame rate fluctuated in the range 40–60 fps due to data bottlenecks. A series of optical filters was used to achieve a working wavelength band of 1500–1700 nm, giving a radiance temperature range of 595–1635 K. The filters used were 2 Thorlabs NENIR10B OD2 neutral density filters, a Thorlabs FEL1500 1500 nm long pass filter and a Thorlabs NF1064-44 44 nm wide notch filter with a 1064 nm centre wavelength. The notch filter was used to provide extra blocking at the laser wavelengths, to remove any reflected light which would be erroneously measured as thermal emission. A 4 mm acrylic window was also mounted to the front of the lens to protect it from spatter.

The setup was calibrated with a Land Instruments Landcal 1200b blackbody furnace and an Isotech miliK with a UKAS calibrated type R

thermocouple. This was accomplished by capturing a series of images of the calibration furnace at approximately 100 K increments between 923 K and 1423 K. The Sakuma-Hattori method was then used to fit a model to these calibration temperature points [34]. This model was used to perform the conversion of raw images from the camera in DLs (Digital Levels), into thermal images. The reported images are in radiance temperature, K_{rad} (i.e. temperature assuming a constant emissivity of 1). The radiance temperature is always lower than the actual temperature, but the scaling is non-linear as described by Planks Law.

The decision to use radiance temperature for analysis steps is considered good practise when working with infrared thermal data because of the large uncertainties associated with emissivity calculation [35]. Where required, emissivity can be applied after any analysis steps

which will reduce the error in the final value [36]. The emissivity of molten material and material undergoing phase changes during a measurement are especially difficult to calculate. This could be due to impurities in the material or changes in the materials surface such as the forming of oxide layers. This is likely the reason for the wide range of emissivity values seen in literature for similar steels [35,37–39].

An emissivity value of 0.14 with an uncertainty of ± 0.1 was chosen for places in this work where it was felt that linking to an absolute temperature was necessary, this is referenced as K_{em} and uncorrected radiance temperatures as K_{rad} . This is slightly lower than other values in the literature but was chosen based on obtaining a realistic melt pool size from the images. The comparison between K_{em} and K_{rad} is seen in Fig. 1d, along with the error in K_{em} , associated with the uncertainty in emissivity.

Thermal images (Fig. 1b) were further analysed using MATLAB® R2019a (Mathworks Inc). The final hatch of each layer was the closest to the camera, this was used to analyse melt pool characteristics. For each layer, a frame was manually identified with the melt pool in the centre of the last hatch. Thermal data was only captured for 30% of Wall B, so this will be omitted in further analysis.

2.3.1. Melt pool dimensions

In the last hatch, the melt pool moves right to left, allowing the depth and length of the melt pool to be seen (Fig. 1). Since the emissivity (0.14) was selected to ensure that all analysed images captured a melt pool of a realistic size, the emissivity corrected liquidus ($1708 K_{em}$ [40]; $1249 K_{rad}$) was used as the melt pool threshold. The melt pool depths calculated with this threshold were 0.88 ± 0.37 mm (standard deviation) similar to the laser diameter.

A contour at the threshold was assumed to be representative of the melt pool. The melt pool area (in mm^2), length (mm) and depth (mm) were calculated for each layer. Spatter could be above the melt threshold (Fig. 1b). To avoid this being counted, the contour with the longest boundary was selected. With a scaling of $1 \text{ px} = 0.37$ mm, an uncertainty of 0.37 mm is associated with the distance measurements.

2.3.2. Extracting cooling rate

To calculate the cooling rate, the centre of the melt pool determined above was found. The location of this pixel was saved along with its temperature. To capture the cooling, the temperature of the same pixel was extracted in subsequent frames (Fig. 1c). Since the frame rate is known, this results in a plot of temperature against time (Fig. 1d). The nearest temperature values either side of the solidus ($1675 K_{em}$ [40]; $1231 K_{rad}$) were found and a cooling rate was determined by dividing the temperature difference by the time difference. A cooling rate was determined for every layer of every wall. In the case that the recorded temperature never reached the solidus, no cooling rate was recorded.

As the laser passes, a plateau of maximum temperature is often experienced before cooling occurs. At high cooling rates, the maximum temperature may only be experienced in one frame. This peak may be an average of the plateau and the start of cooling, or the end of the heating period overlapping with the plateau. If the peak temperature is used in the cooling rate calculation, the error would be increased as the accuracy of the peak point is unknown. Low H samples experience the lowest peak temperatures, so will have the highest cooling rate errors. Finally, the smallest melt pool depths are 2–3 pixels; the pixel analysed for cooling rate calculation is bound to be near a melt pool edge. Due to melt pool fluctuations, the melt pool may deviate outside the tracked pixel leading to an inaccurate cooling rate.

3. Results

3.1. Physical properties

Micrographs were taken of etched samples, approx. 6 layers high and one hatch wide (Fig. 2). Fig. 2a shows Wall A1 (low H), with porosity

visible between the central and the right hand hatches (circled). With a high H (Fig. 2b) no porosity is visible, however, elongated grains can be seen along the centre of the hatch (outlined). The average porosity of a wall decreases with increasing H (Table 2). Average hardness values are shown for each wall and are similar to literature values [20]; walls with a low H have higher hardness. The higher H walls (Walls C and D) have a greater uncertainty in measured hardness, suggesting that hardness is variable within the sample.

Splitting the hardness average into 5 values, each 2 mm tall shows the variation of wall hardness with height. Low H samples (Walls A1, A2 and B) have a consistent hardness of 205–210 HV through the full height (Fig. 3). The increased hardness variability observed in Walls C and D is due to a significant decrease in hardness with wall height. The hardness at the base of all walls is similar; the Wall D (highest H) shows the largest change and experiences an 8% decrease in hardness with height.

3.2. Thermal measurement

For low H walls, the melt pool area increases by a factor 2 through the height, plateauing around 0.5 mm^2 (Fig. 4a). Melt pools in high H walls are larger from layer 1, both Walls C and D experiencing a melt pool area increase by a factor of 6. This is the inverse of the relationship seen with hardness.

Cooling rates in low H walls vary between 7000 and 10,000 K_{rad}/s , with quicker cooling typically lower in the walls (Fig. 4b). High H walls have lower cooling rates initially (6000–7000 K_{rad}/s) and drop more significantly with wall height, ending at 2000–3000 K_{rad}/s . Cooling rates in the low H walls have a large scatter, with outliers generally lower than the trend. In high H walls, the cooling rates have significantly less variability.

3.3. Grain structure and texture

Inverse pole figure (IPF) maps in the X direction (laser movement) are shown for a high H and a low H wall (Fig. 5). There is a stark difference between these; in low H wall (Fig. 5a) the grains are fine with little noticeable texture. Some grains sweep into the centreline of the hatches, but few grains are elongated. No crystal orientations are dominant; there is no visible change in microstructure through height. The high H wall (Fig. 5b) shows distinct elongated grains along the Z direction in the centre of each hatch. These tend to be between the $\langle 100 \rangle$ and the $\langle 111 \rangle$ directions and become larger and more prevalent towards the top of the wall. Between the hatch centres are wide

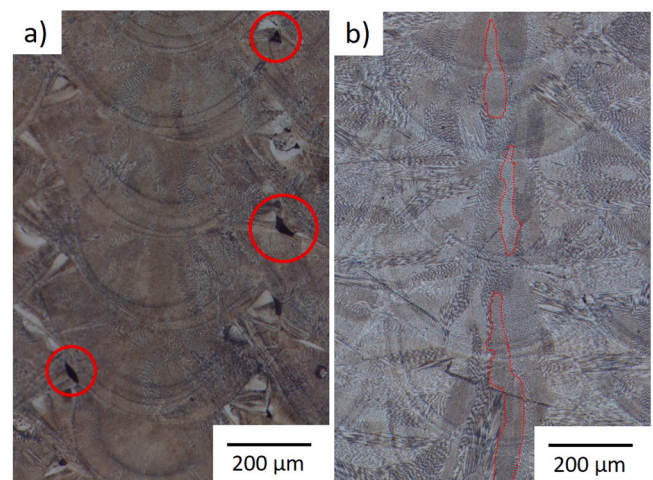


Fig. 2. Optical micrographs of YZ plane of walls etched with aqua regia. a) Wall A1 with examples of porosity circled, b) Wall C with several columnar grains highlighted.

Table 2

Porosity and hardness measurements of walls. Hardness values include a 95% confidence interval.

Sample	H (J/mm)	Porosity (%)	Average hardness (HV)
Wall A1	6.5	0.301	207.6 ± 2.5
Wall A2	6.5	0.259	207.9 ± 2.2
Wall B	8.0	0.182	208.4 ± 2.6
Wall C	10.9	0.081	200.1 ± 3.7
Wall D	13.3	0.105	190.0 ± 3.9

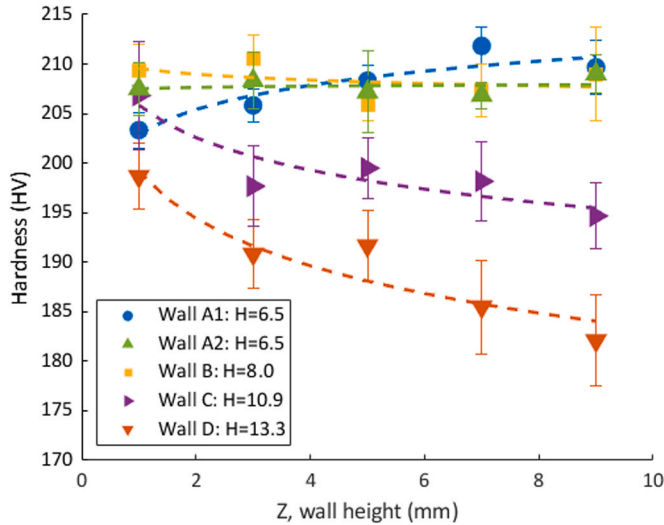


Fig. 3. Hardness variation with wall height. Error bars show standard deviation.

grains aligned in the Y direction, some of these sweep into centreline grains. Very few grains are in $\langle 111 \rangle$ directions.

There is a large variation in grain size between samples, Walls A1 and B (low H) have smaller average grain size and less variation than high H walls (Table 3). Grain size tends to increase with wall height and heat input. The maximum grain size in the centres of low H walls is 20 μm smaller than in the high H walls.

For each wall, inverse pole figures are shown for the X, Y and Z directions (Fig. 6), axes defined in Fig. 1. Since grains are irregular shapes and their crystallographic orientations have three components, the inverse pole figures for the three principal directions can vary significantly. For low H walls (A1, B), there is little texture, the maximum being 2 times the uniform distribution. No texture is in the $\langle 001 \rangle$ directions; this could be linked to the largest cooling gradients which occur at an angle to the defined axes. In high H walls (C, D), the Y direction is heavily textured, which corresponds with literature [11,14]. In the X and Z directions, there is texture in the $\langle 113 \rangle$ direction (between $\langle 001 \rangle$ and $\langle 111 \rangle$, circled in Fig. 6D-C). This equates to 65° above the horizontal. Wall D (highest H), has the strongest texture in both the $\langle 100 \rangle$ direction in the Y orientation and the $\langle 113 \rangle$ direction in the X and Z orientations.

Averaging the anisotropy factor using Eq. (1) for each scanned point within an IPF map, a cumulative anisotropy factor was calculated for each wall in each orientation (Table 4). Due to the strong $\langle 100 \rangle$ texture in the high H walls (in the Y orientation), these have a low average anisotropy factor of 0.13 and 0.10 for Walls C and D respectively. The other orientations on these walls all have anisotropy factors of 0.18–0.19. In low H walls, the average anisotropy factors are 0.21–0.23 in all orientations.

The ratios between the maximum and minimum anisotropy factors for each wall will be referred to as anisotropy variation (Table 4). Low H walls may have higher anisotropy factors, but the anisotropy variation

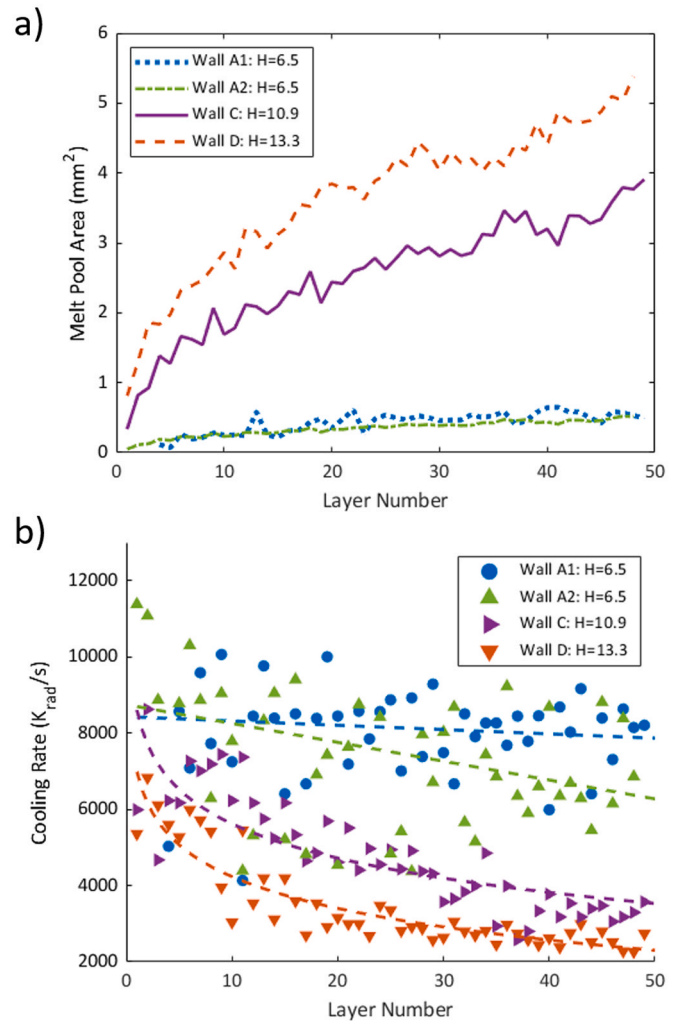


Fig. 4. Thermal variation through layers a) melt pool area; b) cooling rate, dashed lines indicating general trends.

between orientations (within a single IPF map) is minimal. Whereas the high H walls have lower anisotropy, but this varies more between the 3 orientations. The anisotropy factor is not seen to change significantly with height in the low H Wall. There is a noticeable reduction in the anisotropy factors of high H walls with increased height (in all orientations). By taking a ratio of the highest anisotropy factor to the lowest for walls A1 and D (for all three heights), global anisotropy variations can be defined. The global anisotropy variation in Wall A1 (low H) was 1.1, compared to 2.0 for Wall D (high H).

Low H walls have little texture in any orientation, with a maximum texture of 2 multiples uniform density (mud). For high H walls, the texture in the Y direction is much higher than the other directions, with this texture increasing with H, up to 3.4 mud. At the bottom of both walls, there is little texture in the indentation (X) direction (Fig. 7), equiaxed grains dominate; the hardness of both walls is similar in this region. The texture in the Y direction of high H walls increases with height. In the low H wall, there is little microstructural variation through the build height, hardness is constant and texture minimal in all three directions.

4. Discussion

4.1. Correlation of thermal signatures

Over the first 20 layers, cooling rates of high H walls decrease to a

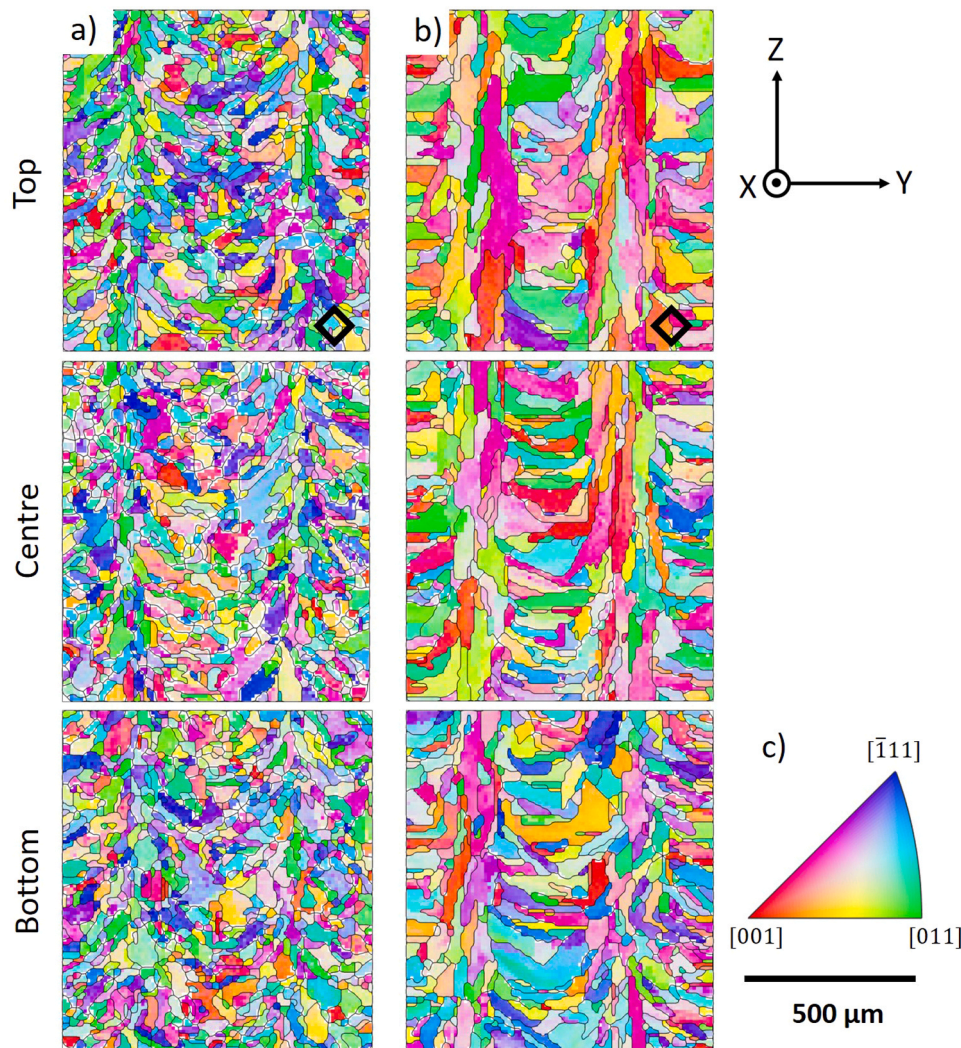


Fig. 5. Inverse pole figure (IPF) maps along X direction of Walls a) A1 (low H); b) D (high H). A top, centre and bottom section of each c) IPF key. Indentation size shown in bottom right corner of each map.

Table 3

Average grain sizes from EBSD scans. For the centre of 4 walls and 3 heights in walls A1 and D.

	Grain Size (Equivalent Radius, μm)	Grain Size Standard Deviation (μm)
Centres		
Wall A1	18.8	8.2
Wall B	19.4	8.7
Wall C	23.2	12.5
Wall D	26.7	16.0
Wall A1		
Top	18.1	8.3
Centre	18.8	8.2
Bottom	17.6	7.9
Wall D		
Top	27.8	17.2
Centre	26.7	16.0
Bottom	23.4	13.0

plateau (Fig. 4b), this is less pronounced in low H walls. This is attributed to the change in heat conduction mode; initially the baseplate is near and conducts heat away quickly. As the wall height increases, heat builds up in the wall and there is a much smaller conduction area – the area of the wall rather than the baseplate. This increases the base material temperature and reduces the cooling rate. Walls A1 and A2 were

built with the same parameters but cooling rates appear to have a large amount of scatter as explained in Section 2.3.2. Due to the rapid heating and cooling in this process, the peak temperature likely captures part of the cooling, leading to a measured value lower than expected. This decreases the measured value of the cooling rate when the peak value is near the solidus temperature. Since this is more likely in low H walls, there are anomalous cooling rates for walls A1 and A2 which are much lower than the general trend (Fig. 4b).

Due to the large uncertainty in emissivity corrected temperature (Fig. 1d), these were not used to calculate cooling rates. Radiance temperature values were used for cooling rates, this assumption is common in such circumstances [41], resulting in units of K_{rad}/s . Emissivity corrected cooling rates would have yielded larger values, but by less than a factor 2. The cooling rates experienced are comparable to literature, where values of the order 10^3 – 10^4 K/s are reported [1,4].

High H walls experience a large decrease in cooling rate through height (Fig. 3) and have the most significant decrease in hardness. Conversely, the low H walls have a more consistent melt pool area and a constant hardness throughout. Hardness increases with cooling rate and decreases with melt pool area. The gradient of 1.05 on a log-log plot shows that the relationship is $\frac{dT}{dt} \propto MP^{-n}$ where MP is the melt pool length (Fig. 8). This was plotted for wall D as the largest melt pools and highest temperatures will yield lower uncertainties. From Fig. 8, n was calculated to be 1.05, compared to 2.02 reported by Hofmeister et al. [4].

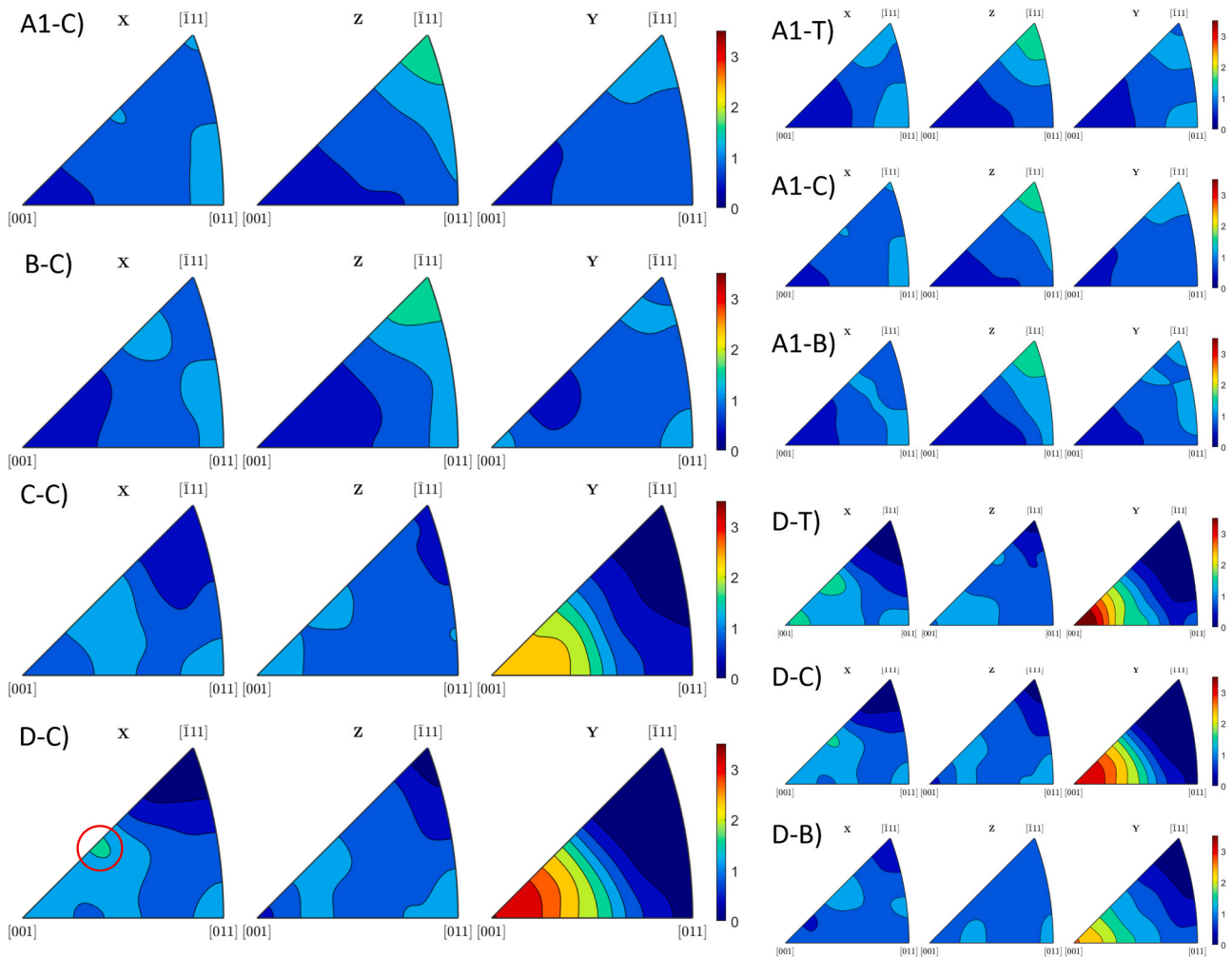


Fig. 6. Inverse pole figures (IPFs) revealing texture of the centre of each wall (left, walls labelled). IPFs of walls A1 and D at the top, centre and bottom (T, C, B respectively). Scale in multiples of uniform density (mud).

Table 4
Average anisotropy factors for 4 walls.

	Average Anisotropy factor (standard deviation)			Anisotropy Variation
	X	Z	Y	
Centres				
Wall A1	0.21 (0.08)	0.23 (0.08)	0.22 (0.08)	1.1
Wall B	0.22 (0.08)	0.22 (0.08)	0.21 (0.09)	1.1
Wall C	0.18 (0.08)	0.19 (0.09)	0.13 (0.08)	1.5
Wall D	0.18 (0.08)	0.19 (0.08)	0.10 (0.07)	1.8
Wall A1				
Top	0.22 (0.08)	0.23 (0.08)	0.22 (0.08)	1.0
Centre	0.21 (0.08)	0.23 (0.08)	0.22 (0.08)	1.1
Bottom	0.22 (0.08)	0.23 (0.08)	0.22 (0.08)	1.1
Wall A1 Global Anisotropy Variation				1.1
Wall D				
Top	0.17 (0.08)	0.18 (0.08)	0.11 (0.07)	1.6
Centre	0.18 (0.08)	0.19 (0.08)	0.10 (0.07)	1.8
Bottom	0.20 (0.08)	0.19 (0.09)	0.15 (0.09)	1.4
Wall D Global Anisotropy Variation				2.0

Since the melt pool length has units of distance, this relationship is equivalent to Chvorinov’s rule, which states that freezing time is proportional to $(Volume/Area)^n$ where n is 1.5–2 [42]. 1.05 doesn’t fit within the range set by Chvorinov’s rule, however this was established for casting and as mentioned, the cooling range value will change dependant on the emissivity chosen.

Since melt pool length is monotonic with cooling rate, it can be used as a proxy for cooling rate; which is beneficial as cooling rates are difficult to measure in-situ. The standard deviation of cooling rates from the line of best fit is found to be 15.5%. Given the melt pool length uncertainty of 0.37 mm and a trendline gradient of -1.05 , the melt pool size uncertainty leads to a cooling rate error of 10.4%, which is similar to the scatter. These calculations were performed for wall D to reduce cooling rate errors due to the measurement limitations, but the conclusions should hold more generally.

From coaxial measurement, literature has reported that the melt pool areas increase with build height. A similar observation has been made in this work but using side-view measurement, showing that the two measurement approaches agree. However, it was also observed that the increase in melt pool area with build height was more pronounced for high H builds compared with low H builds, by a factor of around 3 (Fig. 4a). This suggests that, even for a fixed geometry, the degree of thermal variation through a build (change in melt pool size with build height) is itself dependent on the build parameters. To the authors’ knowledge, this has not been reported previously.

4.2. Grain structure

DED models predict a microstructure containing elongated grains in the Y direction producing the texture seen in high H walls (Fig. 6). There is debate as to what occurs along the centreline. Laser welding literature expects grains to sweep into the centreline and result in elongated grains

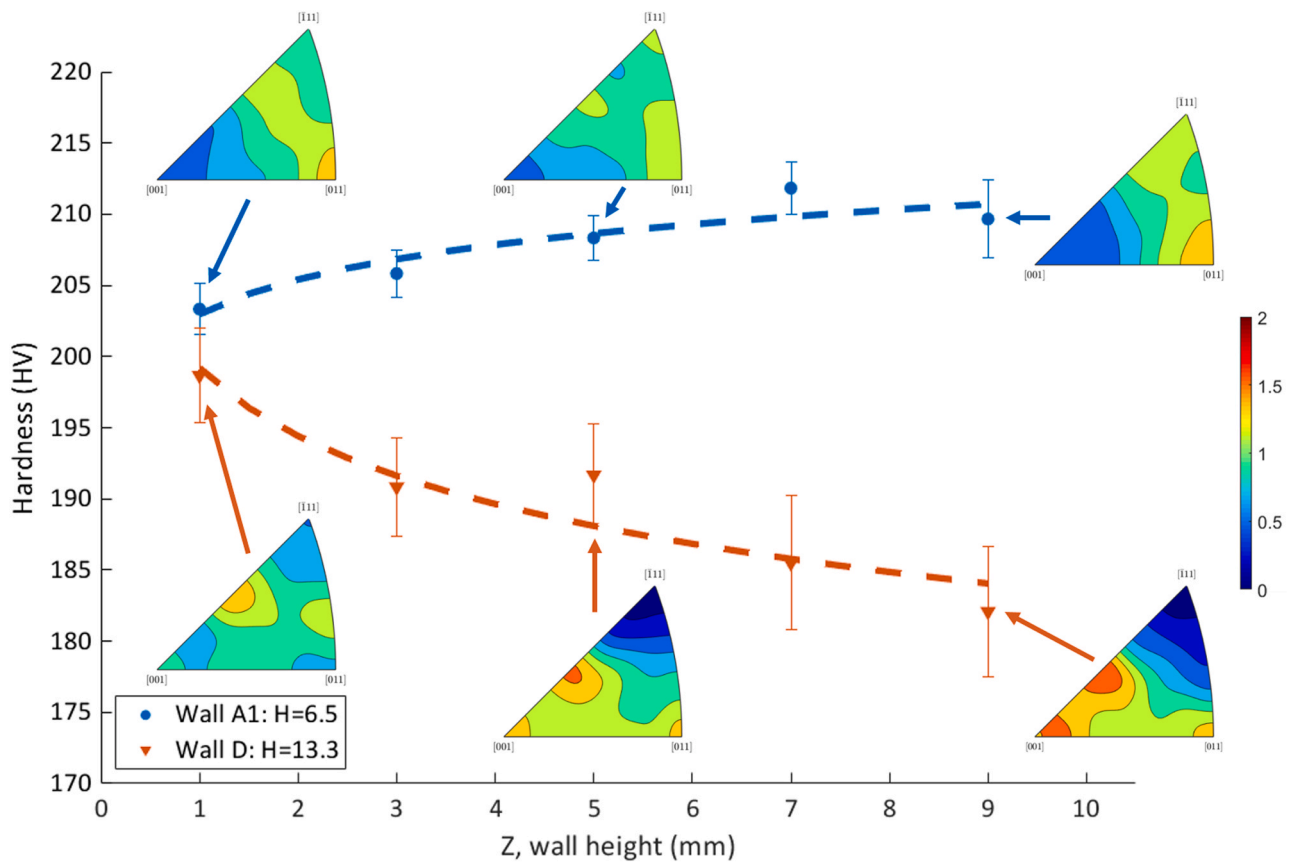


Fig. 7. Variation of hardness through height of walls A1 and D, showing change of texture (in the X direction).

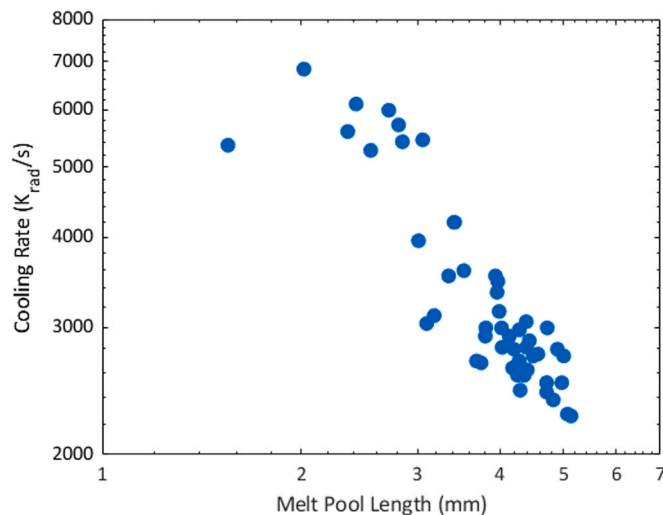


Fig. 8. Cooling rate vs melt pool length for Wall D (log scales).

which lie at 60° between the X and the Z directions, i.e. along the highest thermal gradient [10,13]. These explain the $\langle 113 \rangle$ direction texture seen in high H walls. Other DED models predict equiaxed grains along the centreline, with the equiaxed region expanding at higher velocity (lower H) [11]. This is taken to the extreme in the low H walls, which are mainly equiaxed, with some centreline alignment.

4.3. Effect of anisotropy on hardness

The anisotropy factor, Eq. (1), was developed as a measure of crystal

orientation, as $\langle 111 \rangle$ directions have higher Young's moduli than $\langle 100 \rangle$ directions [21]. This gives a measure of expected mechanical properties for each grain. The hardness indents were performed in the X direction, the average anisotropy factors in this direction were further explored (Table 4). The average anisotropy factor can be shown to scale linearly with both melt pool size and cooling rate.

The Schmid factor describes the ease with which slip will occur; this is calculated for all active slip planes, with the largest Schmid factor being shown (Table 5). The Taylor factor calculates the flow stress due to an applied strain (lower Taylor factor indicates a lower stress required and so a lower hardness). Previous studies have found Schmid to show a weak relationship to hardness, whilst Taylor displays a stronger relationship [43]. Table 5 shows both Taylor and Schmid factors to have a strong correlation with hardness, similar to the anisotropy factor.

The anisotropy factors and hardness's for all of the EBSD scanned regions are in line with literature values (Fig. 9) [20]; anisotropy factor was used because it allows direct comparison to literature. Each hardness indent deforms multiple grains because the indent diagonal is $90\text{--}100\ \mu\text{m}$ (Fig. 5), the resultant hardness is an average hardness across the individual grains. Since literature values were for individual grains, no errors in A_{hkl} were stated.

A small indent allows for analysis of individual grains so a larger hardness difference may be measured between distinct regions; this detail is lost when using a larger indent due to averaging of multiple grains. However, this work focuses on anisotropy differences on the macro-scale, so the large indent is sufficient to provide global trends in hardness and to relate these to the average anisotropy factor.

High H walls have a larger average grain size (Table 3) so fewer grains are deformed by the indenter. This means indents in high H walls deform fewer grains and are less representative, which increases the uncertainty magnitude. The indentation sizes in literature are an order of magnitude smaller than used in this work; so the literature values may

Table 5
Comparison of Schmid and Taylor factors between centres of walls and through the height of Walls A1 and D (standard deviations indicated).

	Schmid Factor	Taylor Factor	Average Anisotropy Factor (X direction)	Hardness (HV)
Centres				
Wall A1	0.451 (0.042)	0.197 (0.047)	0.21 (0.08)	208.3 (1.6)
Wall B	0.450 (0.041)	0.197 (0.048)	0.22 (0.08)	205.8 (1.5)
Wall C	0.461 (0.034)	0.185 (0.054)	0.18 (0.08)	199.5 (3.0)
Wall D	0.464 (0.028)	0.181 (0.055)	0.18 (0.08)	191.7 (3.6)
Wall A1				
Top	0.449 (0.042)	0.200 (0.047)	0.22 (0.08)	209.7 (2.7)
Centre	0.451 (0.042)	0.197 (0.047)	0.21 (0.08)	208.3 (1.6)
Bottom	0.450 (0.042)	0.199 (0.046)	0.22 (0.08)	203.3 (1.8)
Wall D				
Top	0.466 (0.028)	0.177 (0.056)	0.17 (0.08)	182.1 (4.6)
Centre	0.464 (0.028)	0.181 (0.055)	0.18 (0.08)	191.7 (3.6)
Bottom	0.456 (0.038)	0.190 (0.051)	0.20 (0.08)	198.7 (3.3)

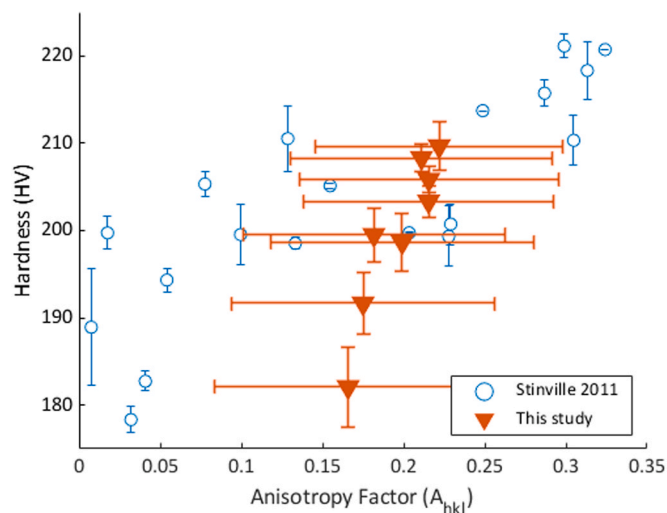


Fig. 9. Change in hardness with anisotropy factor, compared to literature values [20]. Error bars show standard deviation.

overstate the hardness due to the indenter size effect.

Low H walls experienced small melt pools and high cooling rates. Models predict these to experience more equiaxed grains, which have little texture. Since there is no fibre texture, the anisotropy factor is higher and so the walls are harder (Fig. 10). High H walls have larger melt pools, slower cooling rates and larger, more orientated grains. This leads to a more pronounced texture and so a lower anisotropy factor as confirmed by the reduced hardness in the X axes as compared to low H walls (Fig. 10).

Similar variations are seen through the build height. Low H walls have constant melt pool size and cooling rate; this is reflected in a consistent anisotropy factor through build height. The equiaxed nature is shown by the small anisotropy variation. In the high H wall, the melt pool size increases with build height, reducing the cooling rate. This leads to an increase in grain size and a more pronounced texture with build height; the anisotropy factor decreases with height leading to a lower hardness at the top of the walls.

The hardness in each orientation of the wall depends on the average anisotropy factor in that orientation. The severe global anisotropy of the wall could be estimated by taking a ratio between the maximum and minimum anisotropy factors for each wall (Table 4). The low H walls were found to be very isotropic (10% maximum difference in anisotropy factor between orientations in any location). High H walls were found to have a much larger variation (up to 100%), so the mechanical properties

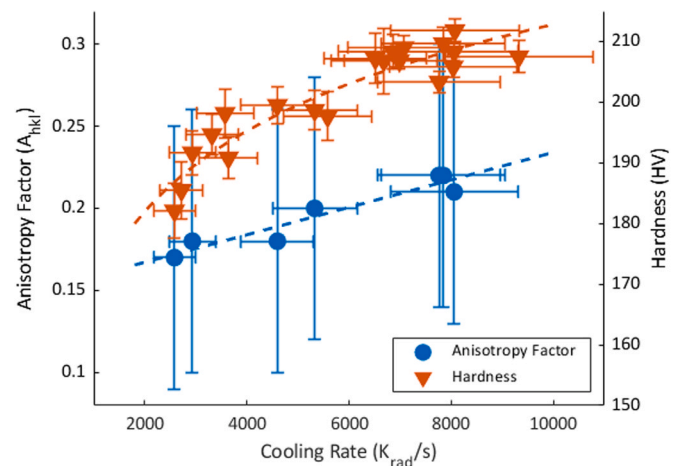


Fig. 10. Variation of anisotropy factor and hardness with cooling rate. Error bars show standard deviation.

in one direction are inferior to those in the other directions. This could create significant issues when producing commercial components, as there are often stringent limits of mechanical properties.

The stark microstructural difference between the low H and the high H walls suggests there was a significant difference in heat flow during manufacture. All walls were built with the same hatch spacing, so the inter-hatch porosity experienced in the low H walls must be due to differences in melt pool width (Fig. 2). The pores between hatches could change the way the heat conducted away from the melt pool. Despite low H walls having better mechanical properties, having regular pores could be a source of mechanical failure which would not be captured in the hardness data.

The optimum wall would have no inter-hatch porosity, like the high H walls, but the isotropic hardness properties of the low H walls. Using a narrower hatch spacing and a closed loop control this could be achieved. It has been shown in this work that the hardness is dependent on the microstructure, which itself is dependent on the cooling rate as summarised in Fig. 10. Since melt pool length/area are monotonic with cooling rate (Fig. 8), control of these would suffice. A coaxial camera would be able to capture this data and so would be the simplest way of achieving these optimal properties.

5. Conclusion

The relationship between cooling rate and melt pool size have been confirmed in DED using a side-on camera. High linear heat input walls are shown to have slower cooling rates, which leads to a more textured grain structure. By calculating the anisotropy factors of individual grains, the measured hardness can be explained through the grain structure which itself is dependent on the cooling rate.

Low linear heat input walls are shown to have both higher hardness and to be more isotropic in terms of their grain structure, with minimal variation through height. High linear heat input wall have an increasing thermal signal with height; this increased temperature creates local anisotropy. The increase in temperature with height is much more significant in the high H walls, so this creates further anisotropy throughout the sample.

The ability to predict the hardness from the thermal signal opens the possibility to tailor mechanical properties throughout a component by setting thermal targets. This is of high importance for acceptance into industrial repair applications, as thermal monitoring can increase confidence in the final components without the need for further testing.

CRedit authorship contribution statement

Lova Chechik: Conceptualization, Methodology, Investigation, Writing - original draft. **Nicholas Andrew Boone:** Investigation, Data curation. **Leigh Russell Stanger:** Investigation, Data curation. **Peter Honniball:** Investigation. **Felicity Freeman:** Conceptualization. **Gavin Baxter:** Supervision. **Jon Raffae Willmott:** Conceptualization. **Iain Todd:** Conceptualization, Supervision.

Declaration of Competing Interest

The authors declare that they have no known competing financial interests or personal relationships that could have appeared to influence the work reported in this paper.

Data availability

Data supporting this publication can be freely downloaded from <https://doi.org/10.5281/zenodo.4312780> under the terms of the Creative Commons Attribution (CC BY) licence.

Acknowledgements

Thanks to Jiawei Xi for providing insight into EBSD processing. This work was supported by the EPSRC Rolls-Royce Strategic Partnership Grant, MAPP (grant EP/P006566/1) and EPSRC (grant EP/R512175/1). The provision of materials and supporting information from Rolls-Royce plc. is gratefully acknowledged. We also wish to acknowledge the Henry Royce Institute for Advanced Materials, funded through EPSRC grants EP/R00661X/1, EP/S019367/1, EP/P02470X/1 and EP/P025285/1, for BeAM Magic 2.0 access at The University of Sheffield.

References

- 1] T. DebRoy, H.L. Wei, J.S. Zuback, T. Mukherjee, J.W. Elmer, J.O. Milewski, A. M. Beese, A. Wilson-Heid, A. De, W. Zhang, Additive manufacturing of metallic components – process, structure and properties, *Prog. Mater. Sci.* 92 (2018) 112–224, <https://doi.org/10.1016/j.pmatsci.2017.10.001>.
- 2] L.L. Parimi, G. Ravi, D. Clark, M.M. Attallah, Microstructural and texture development in direct laser fabricated IN718, *Mater. Charact.* 89 (2014) 102–111, <https://doi.org/10.1016/j.matchar.2013.12.012>.
- 3] G.P. Dinda, A.K. Dasgupta, S. Bhattacharya, H. Natu, B. Dutta, J. Mazumder, Microstructural characterization of laser-deposited Al 4047 alloy, *Metall. Mater. Trans. A Phys. Metall. Mater. Sci.* 44 (2013) 2233–2242, <https://doi.org/10.1007/s11661-012-1560-3>.
- 4] W. Hofmeister, M. Griffith, M. Ensz, J. Smugeresky, Solidification in direct metal deposition by LENS processing, *JOM* 53 (2001) 30–34, <https://doi.org/10.1007/s11837-001-0066-z>.
- 5] G. Bi, A. Gasser, K. Wissenbach, A. Drenker, R. Poprawe, Characterization of the process control for the direct laser metallic powder deposition, *Surf. Coat. Technol.* 201 (2006) 2676–2683, <https://doi.org/10.1016/j.surfcoat.2006.05.006>.
- 6] L. Han, K.M. Phatak, F.W. Liou, Modeling of laser deposition and repair process, *J. Laser Appl.* 17 (2005) 89–99, <https://doi.org/10.2351/1.1848523>.
- 7] T. Stockman, C. Knapp, K. Henderson, J. Carpenter, J. Schneider, Stainless steel 304L LENS AM process monitoring using in-situ pyrometer data, *JOM* 70 (2018) 1835–1843, <https://doi.org/10.1007/s11837-018-3033-7>.
- 8] R.P. Mudge, N.R. Wald, Laser engineered net shaping advances additive manufacturing and repair, *Weld. J.* 86 (2007) 44–48.
- 9] N. Shamsaei, A. Yadollahi, L. Bian, S.M. Thompson, An overview of Direct Laser Deposition for additive manufacturing; Part II: mechanical behavior, process parameter optimization and control, *Addit. Manuf.* 8 (2015) 12–35, <https://doi.org/10.1016/j.addma.2015.07.002>.
- 10] O. Hunziker, D. Dye, R.C. Reed, On the formation of a centerline grain boundary during fusion welding, *Acta Mater.* 48 (2000) 4191–4201, [https://doi.org/10.1016/S1359-6454\(00\)00273-1](https://doi.org/10.1016/S1359-6454(00)00273-1).
- 11] W. Li, M. Soshi, Modeling analysis of the effect of laser transverse speed on grain morphology during directed energy deposition process, *Int. J. Adv. Manuf. Technol.* 103 (2019) 3279–3291, <https://doi.org/10.1007/s00170-019-03690-6>.
- 12] L.E. Criales, Y.M. Arisoy, B. Lane, S. Moylan, A. Donmez, T. Özel, Laser powder bed fusion of nickel alloy 625: Experimental investigations of effects of process parameters on melt pool size and shape with spatter analysis, *Int. J. Mach. Tools Manuf.* 121 (2017) 22–36, <https://doi.org/10.1016/j.ijmactools.2017.03.004>.
- 13] H.L. Wei, J. Mazumder, T. DebRoy, Evolution of solidification texture during additive manufacturing, *Sci. Rep.* 5 (2015) 1–7, <https://doi.org/10.1038/srep16446>.
- 14] G.P. Dinda, A.K. Dasgupta, J. Mazumder, Texture control during laser deposition of nickel-based superalloy, *Scr. Mater.* 67 (2012) 503–506, <https://doi.org/10.1016/j.scriptamat.2012.06.014>.
- 15] S. Chen, G. Guillemot, C.A. Gandin, Three-dimensional cellular automaton-finite element modeling of solidification grain structures for arc-welding processes, *Acta Mater.* 115 (2016) 448–467, <https://doi.org/10.1016/j.actamat.2016.05.011>.
- 16] G. Bi, A. Gasser, Restoration of nickel-base turbine blade knife-edges with controlled laser aided additive manufacturing, *Phys. Procedia* 12 (2011) 402–409, <https://doi.org/10.1016/j.phpro.2011.03.051>.
- 17] D.R. Feenstra, V. Cruz, X. Gao, A. Molotnikov, N. Biribilis, Effect of build height on the properties of large format stainless steel 316L fabricated via directed energy deposition, *Addit. Manuf.* 34 (2020), 101205, <https://doi.org/10.1016/j.addma.2020.101205>.
- 18] J.T. Hofman, B. Pathiraj, J. Van Dijk, D.F. De Lange, J. Meijer, A camera based feedback control strategy for the laser cladding process, *J. Mater. Process. Technol.* 212 (2012) 2455–2462, <https://doi.org/10.1016/j.jmatprotec.2012.06.027>.
- 19] M.L. Griffith, M.T. Ensz, J.D. Puskar, C.V. Robino, J.A. Brooks, J.A. Philliber, J. E. Smugeresky, W.H. Hofmeister, Understanding the microstructure and properties of components fabricated by laser engineered net shaping (LENS), *MRS Proc.* 625 (2000) 9, <https://doi.org/10.1557/PROC-625-9>.
- 20] J.C. Stinville, C. Tromas, P. Villechaise, C. Templier, Anisotropy changes in hardness and indentation modulus induced by plasma nitriding of 316L polycrystalline stainless steel, *Scr. Mater.* 64 (2011) 37–40, <https://doi.org/10.1016/j.scriptamat.2010.08.058>.
- 21] M.T. Hutchings, P.J. Withers, T.M. Holden, T. Lorentzen, Introduction to the Characterization of Residual Stress By Neutron Diffraction, 2005.
- 22] J.J. Roa, G. Fargas, A. Mateo, E. Jiménez-Piqué, Dependence of nanoindentation hardness with crystallographic orientation of austenite grains in metastable stainless steels, *Mater. Sci. Eng. A.* 645 (2015) 188–195, <https://doi.org/10.1016/j.msea.2015.07.096>.
- 23] S. Chen, Y. Miyahara, A. Nomoto, Crystallographic orientation dependence of nanoindentation hardness in austenitic phase of stainless steel, *Philos. Mag. Lett.* 98 (2018) 473–485, <https://doi.org/10.1080/09500839.2019.1577997>.
- 24] T. Miura, K. Fujii, K. Fukuya, K. Takashima, Influence of crystal orientation on hardness and nanoindentation deformation in ion-irradiated stainless steels, *J. Nucl. Mater.* 417 (2011) 984–987, <https://doi.org/10.1016/j.jnucmat.2010.12.197>.
- 25] E. Broitman, Indentation hardness measurements at macro-, micro-, and nanoscale: a critical overview, *Tribol. Lett.* 65 (2017) 1–18, <https://doi.org/10.1007/s11249-016-0805-5>.
- 26] M.H. Farshidianfar, A. Khajepour, A.P. Gerlich, Effect of real-time cooling rate on microstructure in laser additive manufacturing, *J. Mater. Process. Technol.* 231 (2016) 468–478, <https://doi.org/10.1016/j.jmatprotec.2016.01.017>.
- 27] S.J. Wolff, Z. Gan, S. Lin, J.L. Bennett, W. Yan, G. Hyatt, K.F. Ehmann, G.J. Wagner, W.K. Liu, J. Cao, Experimentally validated predictions of thermal history and microhardness in laser-deposited Inconel 718 on carbon steel, *Addit. Manuf.* 27 (2019) 540–551, <https://doi.org/10.1016/j.addma.2019.03.019>.
- 28] J. Yu, X. Lin, J. Wang, J. Chen, W. Huang, Mechanics and energy analysis on molten pool spreading during laser solid forming, *Appl. Surf. Sci.* 256 (2010) 4612–4620, <https://doi.org/10.1016/j.apsusc.2010.02.060>.
- 29] A.R. Rahman Rashid, S. Abaspour, S. Palanisamy, N. Matthews, M.S. Dargusch, Metallurgical and geometrical characterisation of the 316L stainless steel clad deposited on a mild steel substrate, *Surf. Coat. Technol.* 327 (2017) 174–184, <https://doi.org/10.1016/j.surfcoat.2017.08.013>.
- 30] T. Hua, C. Jing, L. Xin, Z. Fengying, H. Weidong, Research on molten pool temperature in the process of laser rapid forming, *J. Mater. Process. Technol.* 198 (2008) 454–462, <https://doi.org/10.1016/j.jmatprotec.2007.06.090>.
- 31] D. Hu, R. Kovacevic, Sensing, modeling and control for laser-based additive manufacturing, *Int. J. Mach. Tools Manuf.* 43 (2003) 51–60, [https://doi.org/10.1016/S0890-6955\(02\)00163-3](https://doi.org/10.1016/S0890-6955(02)00163-3).
- 32] F. Bachmann, R. Hielscher, H. Schaeben, Texture analysis with MTEX- Free and open source software toolbox, *Solid State Phenom.* 160 (2010) 63–68, <https://doi.org/10.4028/www.scientific.net/SSP.160.63>.
- 33] Hamamatsu, InGaAs camera C12741–03, (n.d.). <https://www.hamamatsu.com/resources/pdf/sys/SCAS0111E.C12741-03.pdf> (Accessed June 19 2020).
- 34] F. Sakuma, S. Hattori, Establishing a practical temperature standard by using a narrow-band radiation thermometer with a silicon detector, in: *Temp. Meas. Control Sci. Ind.* 5, 1982, pp. 421–427.
- 35] C. Zhu, M.J. Hobbs, R.C. Masters, C. Rodenburg, J.R. Willmott, An accurate device for apparent emissivity characterization in controlled atmospheric conditions up to 1423 K, *IEEE Trans. Instrum. Meas.* 69 (2020) 4210–4221, <https://doi.org/10.1109/TIM.2019.2944504>.
- 36] P. Saunders, D.R. White, Physical basis of interpolation equations for radiation thermometry, *Metrologia* 40 (2003) 195–203, <https://doi.org/10.1088/0026-1394/40/4/309>.
- 37] H. Fukuyama, H. Higashi, H. Yamano, Thermophysical properties of molten stainless steel containing 5 mass % B4C, *Nucl. Technol.* 205 (2019) 1154–1163, <https://doi.org/10.1080/00295450.2019.1578572>.
- 38] F. Zhang, K. Yu, K. Zhang, Y. Liu, K. Xu, Y. Liu, An emissivity measurement apparatus for near infrared spectrum, *Infrared Phys. Technol.* 73 (2015) 275–280, <https://doi.org/10.1016/j.infrared.2015.10.001>.
- 39] R.V. Tompson, G.K. Tushar, H. Jo, S.K. Loyalka, K. Sridharan, D.S. Viswanath, Long-term prediction of emissivity of structural materials for high temperature reactor systems, 2018. <https://doi.org/10.2172/1463106>.
- 40] P. Pichler, B.J. Simonds, J.W. Sowards, G. Pottlacher, Measurements of thermophysical properties of solid and liquid NIST SRM 316L stainless steel,

- J. Mater. Sci. 55 (2020) 4081–4093, <https://doi.org/10.1007/s10853-019-04261-6>.
- [41] P. Saunders, Radiation thermometry: Fundamentals and applications in the petrochemical industry, 2007. <https://doi.org/10.1117/3.741687>.
- [42] J.T. Black, R.A. Kosher, Degramo's Materials and Processes in Manufacturing, 2012. <https://doi.org/10.1017/CBO9781107415324.004>.
- [43] X. Wang, J.A. Muñoz-Lerma, O. Sanchez-Mata, S.E. Atabay, M. Attarian Shandiz, M. Brochu, Single-crystalline-like stainless steel 316L with different geometries fabricated by laser powder bed fusion, Prog. Addit. Manuf. 5 (2020) 41–49, <https://doi.org/10.1007/s40964-020-00123-9>.